Parity-breaking flows in precessing spherical containers

R. Hollerbach,[1,2] C. Nore,[3,4,5] P. Marti,[1,6] S. Vantieghem,[1] F. Luddens,[3,4,5,7] and J. Léorat[8]

[1]*Institute of Geophysics, ETH Zürich, Sonneggstrasse 5, 8092 Zürich, Switzerland*

[2]*Department of Applied Mathematics, University of Leeds, Leeds LS2 9JT, United Kingdom*

[3]*Laboratoire d'Informatique Pour la Mécanique et les Sciences de l'Ingénieur, CNRS UPR 3251, BP 133, F-91403 Orsay cedex, France*

[4]*Université Paris-Sud 11, 91405 Orsay cedex, France*

[5]*Institut Universitaire de France, 103 bd Saint Michel, 75005 Paris, France*

[6]*Department of Applied Mathematics, University of Colorado, Boulder, Colorado 80309-0526, USA*

[7]*Department of Mathematics, Texas A&M University, College Station, Texas 77843-3368, USA*

[8]*Observatoire de Paris-Meudon, place Janssen, 92195 Meudon, France*

(Received 5 March 2013; published 28 May 2013)

We present numerical solutions of the flow in precessing spheres and spherical shells with small ($r_i/r_o = 0.1$) inner cores and either stress-free or no-slip inner boundary conditions. For each of these three cases we consider the sequence of bifurcations as the Reynolds number $\mathrm{Re} = r_o^2\Omega/\nu$ is increased up to ∼1280, focusing particular attention on bifurcations that break the antipodal symmetry $\mathbf{U}(-\mathbf{r}) = -\mathbf{U}(\mathbf{r})$. All three cases have steady and time-periodic symmetric solutions at smaller Re, and quasiperiodic asymmetric solutions at larger Re, but the details of the transitions differ, and include also periodic asymmetric and quasiperiodic symmetric solutions in some of the cases.

DOI: 10.1103/PhysRevE.87.053020 PACS number(s): 47.20.Ky, 47.11.−j

I. INTRODUCTION

A rotating solid object is said to precess when its rotation axis itself rotates (typically at a much slower rate) about a secondary axis that is fixed in an inertial reference frame. If the rotating object is a fluid-filled container, very complicated fluid flows may be generated. The first theoretical studies of precession-driven flows were by Sloudsky in 1895 [1] and Poincaré in 1910 [2], who were interested in flows induced in the interiors of precessing planets or stars. This so-called Poincaré solution consists of an essentially solid-body rotation, but about an axis that always lags slightly behind the instantaneous rotation axis of the spheroidal container. Further refinements to the Poincaré flow include viscous effects [3,4], and continue to this day [5].

Based on the Poincaré flow and its lack of sufficiently complicated structure, Bullard in 1949 [6] suggested that precession was unlikely to be the origin of the Earth's magnetic field. He acknowledged though that the Poincaré flow could well be unstable, in which case there could be substantial small-scale structures after all. The pioneering experiments by Malkus in 1968 [7] on precessing spheroids revealed this to be the case, and since then it has been accepted that the geodynamo could be at least partially driven by precession (with convection-driven flows the alternative). The instabilities of the Poincaré flow are by now well understood in terms of resonant coupling of a pair of inertial waves [8,9].

Following Malkus, there have been a number of further experiments involving precessing spheroids [10–13], triaxial ellipsoids [14], spheres [15,16], and spherical shells [17], spanning the entire range from the Poincaré solution and slight deviations from it observed for very slow precession all the way to fully developed turbulence observed for rapid precession. Related theoretical and numerical work [5,18–25] similarly covers a broad range of phenomena obtained at different rotation and precession rates.

Regarding the origin of the Earth's magnetic field, the possibility of precession-driven dynamo action was first demonstrated numerically by Tilgner [26,27] in a sphere, and by Wu and Roberts [28] in a spheroid. Very recently, Dwyer *et al*. [29] have also suggested that the Moon may once have had a precession-driven dynamo. Another possible astrophysical application of (nonmagnetic) precession-driven flows is in the interiors of neutron stars, where Glampedakis *et al*. [30] suggest that certain instabilities must be taken into account in interpreting the observed precession of radio pulsars.

In this paper we will focus on one particular aspect of the problem, namely, the parity, or symmetry, on reflection through the origin. The basic nature of the forcing is such that solutions exist satisfying

$$\mathbf{U}(-\mathbf{r}) = -\mathbf{U}(\mathbf{r}), \tag{1}$$

where $\mathbf{r}$ is the position vector, and $\mathbf{U}$ the fluid flow. For sufficiently strong forcing these pure-parity solutions may become unstable though, giving rise to mixed-parity solutions that no longer satisfy (1). It is then of interest to consider the precise sequence of bifurcations whereby the solutions gradually acquire more and more structure, including breaking the symmetry (1). Indeed, Refs. [26–28] all suggest that mixed-parity flows are more efficient dynamos than pure-parity ones.

A further issue that we will explore concerns the difference between a full sphere and a spherical shell. It is well known that inertial waves in general behave very differently in the two geometries [31,32], and even that the internal shear layers associated specifically with the precessional spin-over mode behave differently [33,34]. Given such differences between the two geometries, even regarding purely linear phenomena, as both of these are, it is of interest to investigate how different they may be regarding intrinsically nonlinear phenomena such as parity-breaking bifurcations.

II. EQUATIONS

Let $\hat{\mathbf{e}}_p$ be a unit vector defining the precession axis (which we recall is fixed in the inertial frame). In the reference frame

rotating about $\hat{\mathbf{e}}_p$ at the precession rate Ω_p, the container rotates about a fixed axis, at a constant rate Ω. Denote this rotation axis as the z axis, and define a complete Cartesian coordinate system (x,y,z) such that

$$\hat{\mathbf{e}}_p = \sin\alpha\hat{\mathbf{e}}_x + \cos\alpha\hat{\mathbf{e}}_z.$$

That is, α is the angle between the rotation axis $\hat{\mathbf{e}}_z$ and the precession axis $\hat{\mathbf{e}}_p$.

Scaling length by the container's outer radius r_o, time by Ω^{-1}, and $\mathbf{U}$ by $r_o\Omega$, the Navier-Stokes equation in this reference frame becomes

$$\partial_t\mathbf{U} + \mathbf{U}\cdot\nabla\mathbf{U} + 2\epsilon\,\hat{\mathbf{e}}_p\times\mathbf{U} = -\nabla p + \mathrm{Re}^{-1}\nabla^2\mathbf{U}, \qquad (2)$$

with an associated boundary condition

$$\mathbf{U} = \sin\theta\,\hat{\mathbf{e}}_\phi \quad \text{at} \quad r = 1, \qquad (3)$$

where (r,θ,ϕ) are spherical coordinates related to (x,y,z) in the usual way.

The condition (3) applies to both a full sphere and a spherical shell. For the sphere there are no further conditions, but for the shell we also need to specify boundary conditions at the inner radius r_i, which we will fix at $r_i = 0.1$, to focus attention on the effects that even a quite small inner sphere can have. This value was chosen by Tilgner [26] for purely numerical reasons. For the conditions at r_i we will consider two possibilities, namely, stress free,

$$U_r = 0, \quad \partial_r(U_\theta/r) = 0, \quad \partial_r(U_\phi/r) = 0 \quad \text{at} \quad r = r_i,$$

and no slip (with the inner sphere corotating and precessing with the outer sphere),

$$\mathbf{U} = r_i\sin\theta\,\hat{\mathbf{e}}_\phi \quad \text{at} \quad r = r_i.$$

[Note also that stress-free conditions cannot be applied at the outer boundary, as otherwise the fluid would not sense the boundary condition (3). More generally, stress-free boundary conditions in spherical geometry can also lead to difficulties with angular momentum conservation [35], as well as other spurious behaviors [36].]

The three nondimensional parameters defining the problem are the Reynolds number

$$\mathrm{Re} = r_o^2\Omega/\nu$$

measuring the rotation (often also replaced by the Ekman number $E = \mathrm{Re}^{-1}$), the precession rate $\epsilon = \Omega_p/\Omega$, and the precession angle α. We choose to perform a single parameter study varying only the Reynolds number, at the precession parameters $\epsilon = 0.3$ and $\alpha = 120^\circ$ (corresponding to a retrograde precession). The parameters ϵ and α are fixed at these values only because this case was previously considered by Ref. [26], and is therefore a useful starting point to a more detailed exploration. We will then compute the sequence of bifurcations as Re is increased, and consider the similarities and differences between the full sphere and the spherical shell with stress-free and no-slip boundary conditions.

Note finally how the precession is taken into account by the Coriolis force in Eq. (2), whereas the primary rotation is imposed by the inhomogeneous boundary condition (3). Two alternative reference frames would be (i) the inertial frame, in which there would be no Coriolis force, but the boundary condition would be extremely complicated, or (ii) the frame fixed to the container, in which the boundary condition would be homogeneous, but the noninertial effects would be more complicated, involving not only the Coriolis force but also the so-called Poincaré force [7]. The advantage of the reference frame used here is that this is the only frame in which neither the equation nor the boundary condition involve any explicit time dependence, and is therefore the only frame in which the flow can appear steady. If one is interested in studying transitions to increasingly complicated time dependencies, this frame is thus superior to either of the alternatives.

III. NUMERICAL SOLVERS

All calculations presented in this paper were computed by two very different, and independently developed, numerical codes, one based on spherical harmonics [37] (denoted H2000) and one based on spectral/finite elements [38] (denoted SFEMANS). Both codes have the capacity to solve, for example, the magnetic induction equation as well, but here we use them only as Navier-Stokes solvers. Since both codes have been extensively documented in the given references, we only give brief summaries here.

The H2000 code starts with the so-called toroidal-poloidal decomposition $\mathbf{U} = \nabla\times(e\hat{\mathbf{e}}_r) + \nabla\times\nabla\times(f\hat{\mathbf{e}}_r)$, thereby automatically satisfying $\nabla\cdot\mathbf{U} = 0$. The scalar potentials e and f are expanded in terms of spherical harmonics $P_l^m(\cos\theta)\exp(im\phi)$. The r components of the first and second curls of (2) then yield relatively simple evolution equations for the individual harmonics of e and f. Taking curls of (2) also eliminates the pressure, and hence any need for a pressure solver.

The radial structure of e and f is expanded in terms of Chebyshev polynomials. The original H2000 code is valid only in a spherical shell, with the interval $r = [r_i,r_o]$ linearly mapped to the standard Chebyshev range $[-1,1]$. A full sphere version was developed by modifying this to

$$e_{lm}(r) = \sum_k e_{klm}T_{2k-1}(r)r^{l'},$$
$$f_{lm}(r) = \sum_k f_{klm}T_{2k-1}(r)r^{l'}, \qquad (4)$$

where $l' = 1$ or 2 depending on whether the spherical harmonic degree l is odd or even. Compared with the original expansion, the differences are (i) only the odd Chebyshev polynomials $T_{2k-1}(r)$ are used, (ii) only the half range $r = [0,1]$ is used, and (iii) different expansions are used for different spherical harmonics, via this factor $r^{l'}$, ensuring that each mode has the appropriate even or odd radial symmetry required by regularity at the origin.

The SFEMANS code starts with a Fourier expansion in the azimuthal direction, followed by a finite element decomposition in the meridional plane, applied separately to each Fourier mode. Pressure and incompressibility are dealt with by a rotational pressure-correction projection method. See also Refs. [39,40] for similar methods combining Fourier expansions in azimuth with spectral or finite elements in cross section. All such methods are more general than H2000 or other spherical harmonics based codes, since they can deal with any axisymmetric container, not just spheres and spherical shells.

Correspondingly though, such methods are typically also considerably slower than spherical harmonics codes. We use SFEMANS in spherical geometry here primarily for comparison purposes, but its real strength lies in spheroids, or cylinders [41].

Note also that as different as the H2000 and SFEMANS codes are, the basic $\exp(im\phi)$ Fourier expansion in azimuth is common to both, making comparisons of the kinetic energy in a given Fourier mode (for example) particularly easy. In contrast, the parity (1) looks very different in the two codes. In terms of spherical harmonics, solutions satisfying (1) consist of only odd l for e and only even l for f, so parity-breaking bifurcations are easily detected simply by monitoring the energy in the other l modes. In SFEMANS one first separates the flow into so-called symmetric and antisymmetric parts,

$$\mathbf{U}_s = [\mathbf{U}(\mathbf{r}) - \mathbf{U}(-\mathbf{r})]/2, \quad \mathbf{U}_a = [\mathbf{U}(\mathbf{r}) + \mathbf{U}(-\mathbf{r})]/2,$$

and considers the corresponding kinetic energies K_s and K_a.

Typical resolutions for the H2000 code ranged from $(k,l,m) = (30,30,20)$ to $(50,50,30)$. The same $m = 20$–30 range was used for SFEMANS, together with a mesh size in the meridional plane of ~ 0.01 in the interior, and somewhat smaller near the boundaries. Finally, a few limited comparisons were also done with two further codes [42,43]; see also Ref. [44] for more detailed comparisons of these two codes with H2000, SFEMANS, and several other codes in a number of (nonprecessing) benchmark problems.

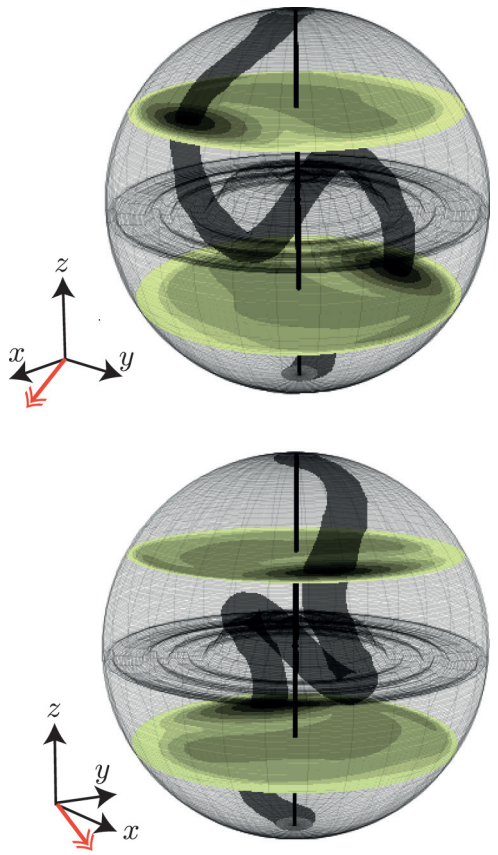

FIG. 1. (Color online) The steady flow for a full sphere at $\mathrm{Re} = 700$, showing isosurfaces of $|\mathbf{U}| = 0.1$ and slices at $z = \pm 0.5$: $|\mathbf{U}|$ varies between 0 (dark) and 1 (light). The rotation axis is Oz, and the precession axis is indicated by a (red) double arrow (120° from the Oz axis). The S-shaped vortex, a characteristic feature of precession-driven flows, is steady in the precessing reference frame. The wireframe shows the spatial domain decomposition used in the SFEMANS code (two meridional domains that are not strictly hemispherical, and with 48 azimuthal modes).

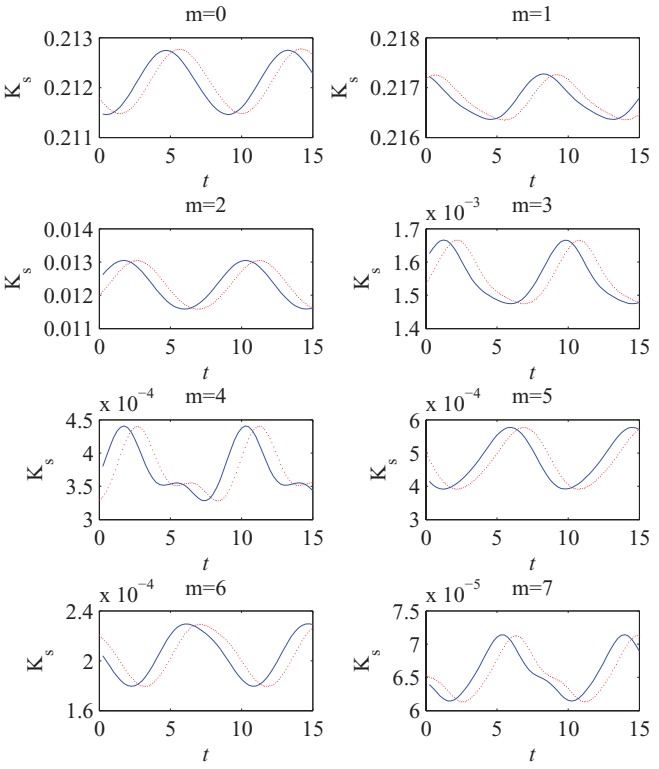

FIG. 2. (Color online) The kinetic energy in the individual Fourier modes $m = 0$–7 as functions of time; the period is $T = 8.7$. The solid (blue) curves are the H2000 results, and the dotted (red) curves the SFEMANS results. $\mathrm{Re} = 910$.

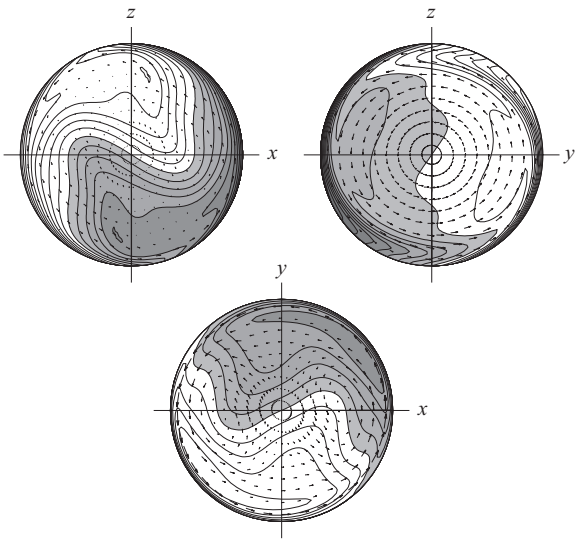

FIG. 3. The time average $\bar{\mathbf{U}}$ of the $\mathrm{Re} = 910$ flow. The three panels denote slices in the xz, yz, and xy planes, as indicated. Within each panel the arrows represent the flow in that plane, and the contours the flow normal to the plane. The contour interval is 0.1, with white indicating negative values and gray positive.

IV. FULL SPHERE RESULTS

The basic sequence of bifurcations for the full sphere can be summarized as follows: (a) Up to Re = 880 the solutions are both steady and symmetric, satisfying (1), (b) for $885 \leqslant \mathrm{Re} \leqslant 1000$ they are periodic in time, but still symmetric, and (c) for $\mathrm{Re} \geqslant 1005$ they are quasiperiodic in time, and asymmetric. In the remainder of this section we will consider the detailed behavior in each of these three regimes.

Figure 1 presents a three-dimensional (3D) plot of the steady solution at Re = 700. A characteristic feature is the S-shaped vortex where the flow speed $|\mathbf{U}|$ is very small. Near the center this vortex is aligned along the precession axis, that is, in the xz plane, at an angle $\alpha = 120^\circ$.

Turning next to the periodic regime, Fig. 2 shows how the kinetic energy varies in time at Re = 910. The agreement between H2000 and SFEMANS is excellent, even for the Fourier

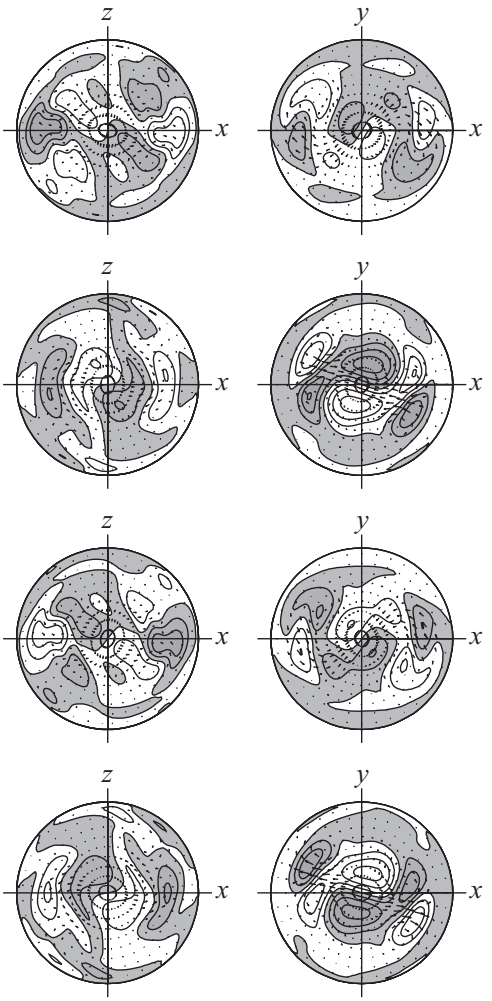

FIG. 4. From top to bottom, four snapshots of $\mathbf{U}' = \mathbf{U} - \bar{\mathbf{U}}$ for the Re = 910 solution. The first snapshot corresponds to the maximum of the $m = 0$ kinetic energy in Fig. 2, the second midway between the maximum and the subsequent minimum, the third the minimum, and the fourth midway between the minimum and the subsequent maximum. The left column shows the xz plane, and the right column the xy plane, as indicated. Arrows and contours as in Fig. 3, but with a contour interval of 0.01, reflecting the much smaller values of $\mathbf{U}'$ compared with $\bar{\mathbf{U}}$.

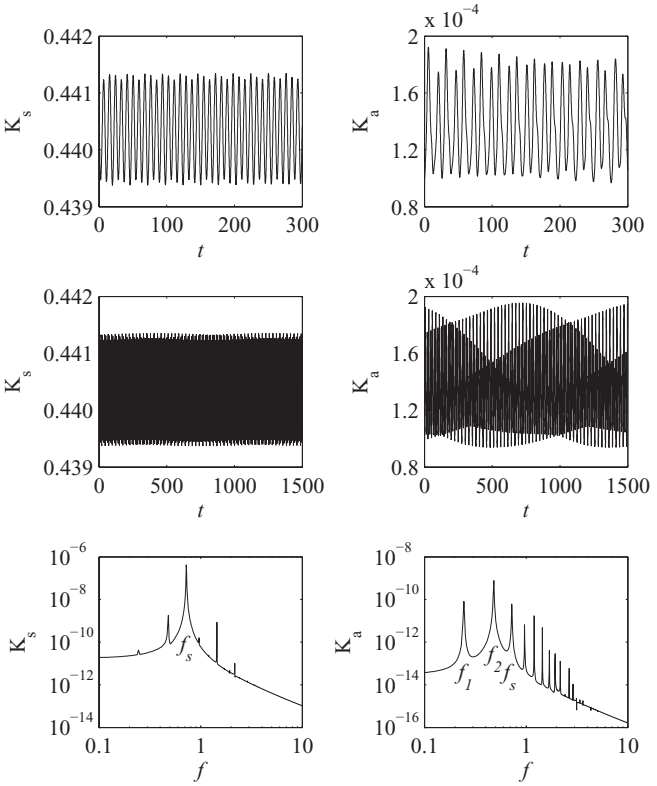

FIG. 5. Time series and Fourier spectra of the kinetic energies K_s (left) and K_a (right). Within each column the first panel shows a relatively short (300) time series, showing the rapid oscillations. The second panel shows a longer (1500) time series, showing the long-term quasiperiodic evolution. The third panel shows the Fourier spectrum of a long time series, indicating the primary oscillation at f_s and the instability pair at f_1 and f_2. Re = 1010.

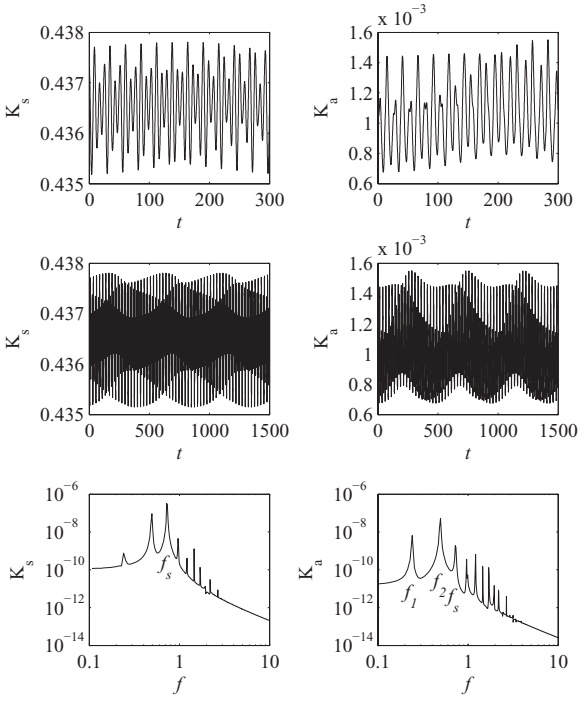

FIG. 6. As in Fig. 5, but at Re = 1100.

mode $m = 7$ (and still higher), where the energy is more than three orders of magnitude reduced from the $m = 0$ and 1 dominant contributions. The phase offset between the two sets of results is of course arbitrary, and was adjusted to make comparison particularly easy.

Figure 3 illustrates the spatial structure of $\bar{\mathbf{U}}$, the flow averaged over the period. The S-shaped vortex from Fig. 1 shows up particularly clearly in the xz plane in the first panel, as the line separating white from gray, where $U_y = 0$ (a backwards S actually). The S-shaped vortex results from the domination of $m = 0$ and $m = 1$ modes and characterizes precession driven flows at small precession rates in various geometries. The "global-rotation" component of the flow is nicely seen in the yz plane in the middle panel.

Figure 4 shows snapshots of $\mathbf{U}' = \mathbf{U} - \bar{\mathbf{U}}$, the time-dependent part of the flow (which is roughly an order of magnitude less than $\bar{\mathbf{U}}$). Comparing the xz and xy planes in Figs. 3 and 4, we see that $\mathbf{U}'$ is concentrated near the S-shaped vortex; the time dependence evidently consists of a periodic "vibration" of this structure. The yz plane exhibits very little activity, and is thus not shown.

Figures 5 and 6 (Re = 1010 and 1100, respectively) indicate the temporal behavior in the quasiperiodic, asymmetric regime. The Fourier spectra of the kinetic energy time series are

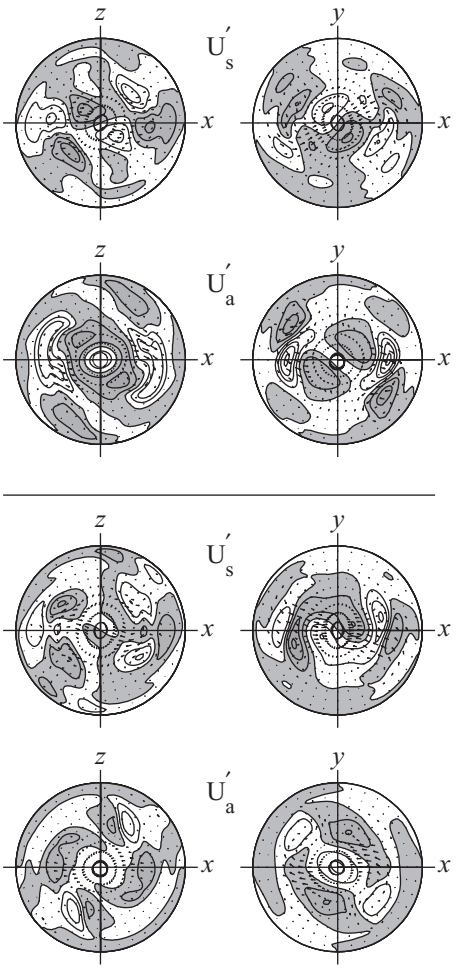

FIG. 7. Two snapshots of $\mathbf{U}'$ for the Re = 1100 solution (with the horizontal line separating the two). The first corresponds to one of the maxima in K_a in Fig. 6, and the second to the subsequent minimum. Within each snapshot the first row shows the $\mathbf{U}'_s$ part of $\mathbf{U}'$ and the second shows $\mathbf{U}'_a$, as indicated. Arrows and contours as in Fig. 4, but with a contour interval of 0.02, reflecting the increase in $\mathbf{U}'$ compared with Re = 910.

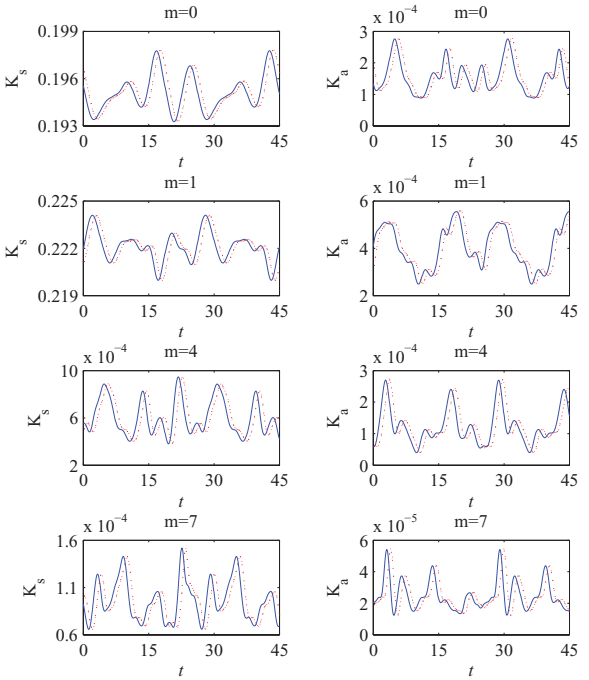

FIG. 8. (Color online) The kinetic energy at Re = 1200, in the Fourier modes $m = 0$, 1, 4, and 7 as functions of time, with the left column showing K_s and the right column K_a. The solid (blue) curves are the H2000 results, and the dotted (red) curves the SFEMANS results. Other Fourier modes agreed equally well.

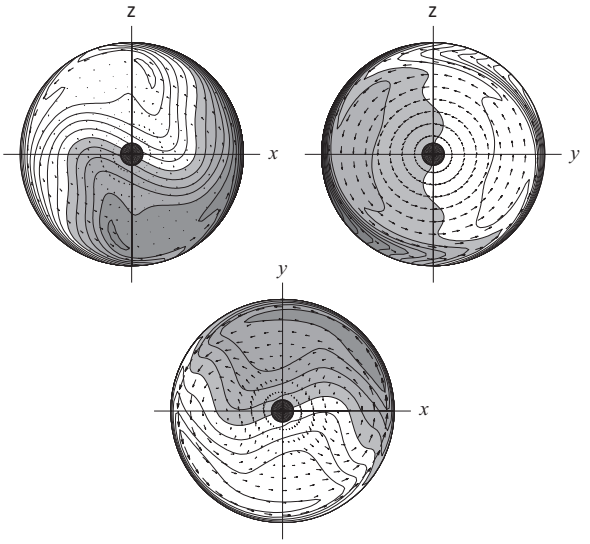

FIG. 9. The time average $\bar{\mathbf{U}}$ of the Re = 1200 flow. The three panels denote slices in the xz, yz, and xy planes, as indicated. Within each panel the arrows represent the flow in that plane, and the contours the flow normal to the plane. The contour interval is 0.1, with white indicating negative values and gray positive. The black dots in the center correspond to the inner sphere.

particularly revealing: Before the bifurcation, $K_a = 0$, and K_s is periodic, with single frequency f_s. The antisymmetric mode then sets in as a pair, f_1 and f_2, satisfying the resonant triad condition $f_1 + f_2 = f_s$. Looking at the specific numbers in more detail, at Re = 1010 we have $f_s = 0.7233$, $f_1 = 0.2435$, and $f_2 = 0.4798$, and at Re = 1100 we have $f_s = 0.7272$, $f_1 = 0.2380$, and $f_2 = 0.4893$. Besides $f_1 + f_2 = f_s$, another point to note is that $f_s \approx 0.72$ is indeed consistent with the period $T = 2\pi/f_s \approx 8.7$ previously seen in Fig. 2.

A less obvious combination to consider is $2f_1 - f_2$, which comes out as 0.0072 at Re = 1010, and -0.0133 at Re = 1100. The significance of these values is twofold. First, the periods corresponding to $2\pi/|2f_1 - f_2|$ are 870 and 470, respectively, which are precisely the very long quasiperiodicities seen in Figs. 5 and 6. Second, if $2f_1 - f_2$ is positive at Re = 1010 and negative at Re = 1100, there must be some intermediate point where it is exactly zero. Together also with $f_1 + f_2 = f_s$, this would imply that $f_2 = 2f_1$ and $f_s = 3f_1$—that is, a periodic solution, where all relevant frequencies are integer multiples of some fundamental frequency f_1. Further investigations revealed this critical point to lie somewhere near Re = 1030. Solutions at Re = 1025 and Re = 1035 were clearly quasiperiodic, indicating that any possible phase locking associated with this critical point extends at most over a very narrow range in Re. We will return to this point in the next section, though. Finally, note that while Figs. 5 and 6 present H2000 results only, the SFEMANS results were again in excellent agreement, exhibiting the same very long quasiperiodicities.

Turning finally to the spatial structures of these mixed-parity, quasiperiodic solutions, the time-averaged flow $\bar{\mathbf{U}}$ is essentially the same as in Fig. 3. In particular, $\bar{\mathbf{U}}$ itself remains symmetric; if the average is taken over several of the long quasiperiodic cycles, its antisymmetric component quickly tends to zero. Figure 7 shows snapshots of the fluctuating part of the flow $\mathbf{U}'$, separated into its symmetric and antisymmetric components. $\mathbf{U}'_s$ is quite similar to some of the structures previously seen in Fig. 4; $\mathbf{U}'_a$ obviously has the opposite parity, but is otherwise concentrated in the same areas. In particular, both $\mathbf{U}'_s$ and $\mathbf{U}'_a$ affect the bulk of the flow, rather than being boundary layer phenomena. The previous vibration of the S-shaped vortex thus becomes asymmetric and quasiperiodic, but is otherwise similar to what it was before the parity-breaking bifurcation.

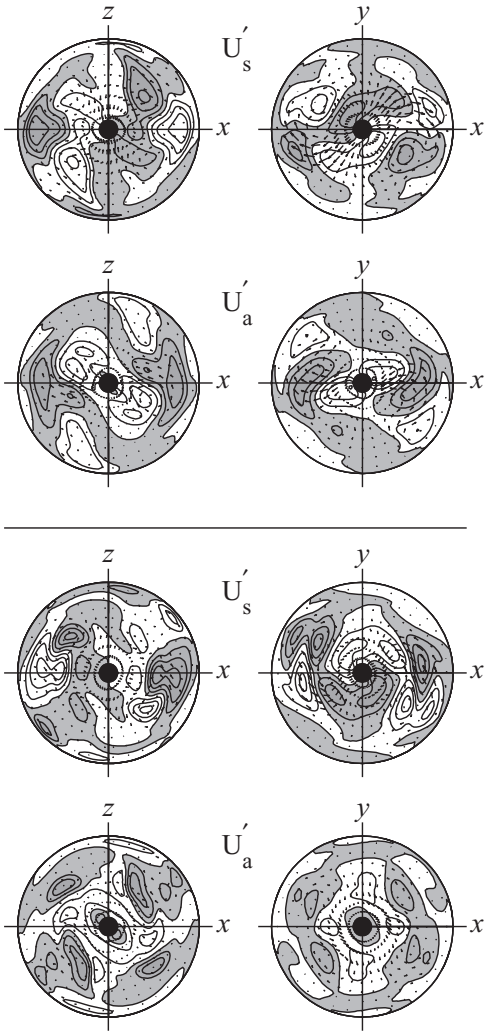

FIG. 10. Two snapshots of $\mathbf{U}'$ for the Re = 1200 solution, at the instants in time where K_s, $m = 0$ has its maximum and minimum values in Fig. 8. These instants were chosen to facilitate comparison with the first and third snapshots in Fig. 4. As in Fig. 7, within each snapshot the first row shows the $\mathbf{U}'_s$ part of $\mathbf{U}'$ and the second $\mathbf{U}'_a$. The contour interval is 0.02 (as in Fig. 7).

V. SPHERICAL SHELL, STRESS-FREE INNER CORE

The initial sequence of bifurcations is very similar to the full sphere case: At Re = 880 the solutions become periodic but still symmetric, and at Re = 1080 they be-

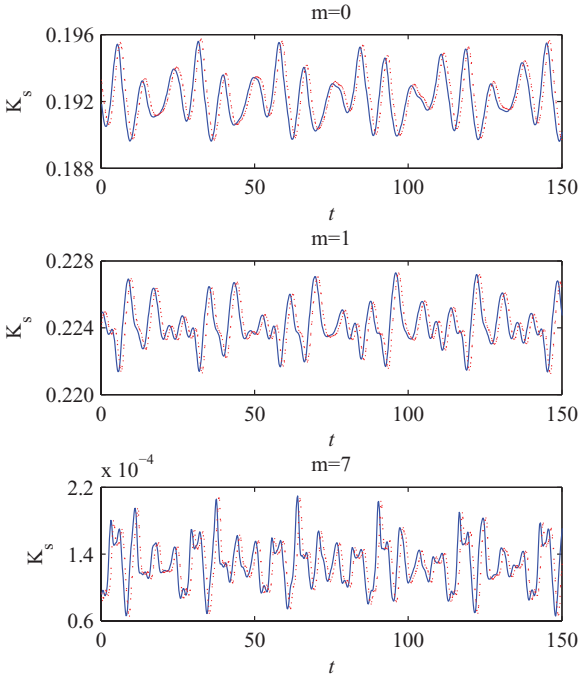

FIG. 11. (Color online) The kinetic energy in the Fourier modes $m = 0$, 1, and 7 as functions of time, for the pure-parity Re = 1270 quasiperiodic solution. The solid (blue) curves are the H2000 results, and the dotted (red) curves the SFEMANS results.

come quasiperiodic and asymmetric. The first bifurcation point is thus virtually identical to its full sphere equivalent (880 vs 885), whereas the second is increased somewhat (1080 vs 1005). The fundamentally different aspect that arises in this case is that now the quasiperiodic regime is interrupted by a—surprisingly large—range where the solutions are phase locked. For $1080 \leqslant \mathrm{Re} \leqslant 1120$ we have quasiperiodicity, with $2f_1 - f_2 > 0$, then for $1125 \leqslant \mathrm{Re} \leqslant 1235$ we have $2f_1 - f_2 = 0$, and hence periodic solutions, then for $\mathrm{Re} \geqslant 1240$ we have quasiperiodicity again, with $2f_1 - f_2 < 0$.

Figure 8 illustrates the periodic nature of the solution at $\mathrm{Re} = 1200$, where the period is $T = 25.9$ (note how this is three times the ∼8.7 period associated with f_s, consistent with $f_1 = f_s/3$). The time dependence of the various Fourier modes is far more complicated than previously shown in Fig. 2, but the agreement between H2000 and SFEMANS is still near perfect. Figure 9 presents the spatial structure of $\bar{\mathbf{U}}$, which again remains symmetric, and is again essentially the same as in Fig. 3. Figure 10 shows snapshots of the fluctuating part of the flow $\mathbf{U}'$. Comparing with Figs. 4 and 7, we recognize many of the same structures.

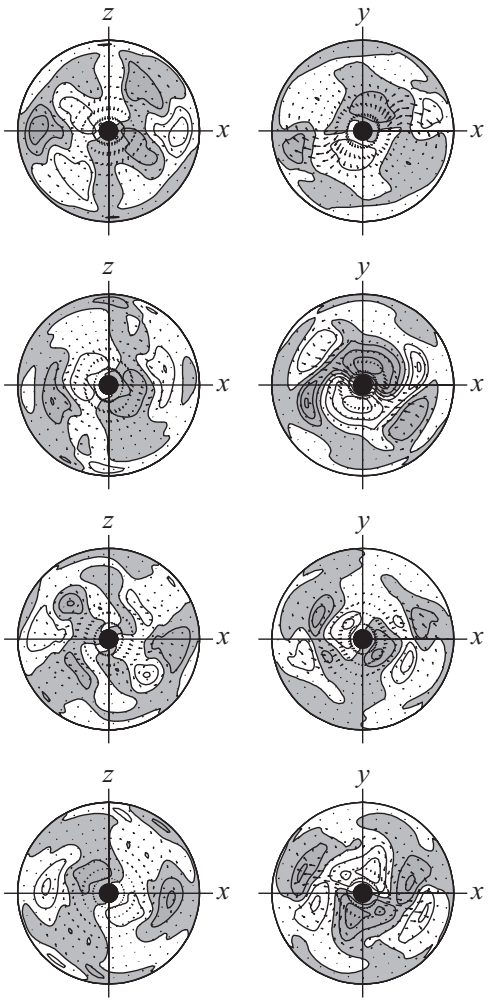

FIG. 12. From top to bottom, four snapshots of $\mathbf{U}'$ for the $\mathrm{Re} = 1270$ pure-parity solution. The first corresponds to the maximum of the $m = 0$ kinetic energy in Fig. 11, the second midway between the maximum and the subsequent minimum, the third the minimum, and the fourth midway between the minimum and the subsequent maximum (compare with Fig. 4). The contour interval is 0.04, reflecting the relatively large fluctuations in this solution.

VI. SPHERICAL SHELL, NO-SLIP INNER CORE

This case is surprisingly different from the previous two. The first bifurcation, from a steady to a periodic but still symmetric solution, occurs much as before, at $\mathrm{Re} = 865$ in this case. The next bifurcation is already different, though: At $\mathrm{Re} = 1190$ the solutions again become quasiperiodic, but this time remain symmetric. As Re is increased still further, these solutions remain linearly stable to antisymmetric perturbations, up to $\mathrm{Re} = 1280$ at least. Beyond this point calculations became increasingly difficult for both H2000 and SFEMANS, with the two codes also no longer agreeing with one another. We cannot say therefore where (if ever) this solution branch becomes linearly unstable to antisymmetric perturbations.

However, by using a suitable initial condition (such as the previous solution in Fig. 10, with the inner boundary conditions adjusted over some suitably short initial time interval) that already contains a significant $\mathbf{U}_a$ contribution, a second solution branch was found that does include antisymmetric components. Once obtained at $\mathrm{Re} = 1280$, this branch could be tracked back down to $\mathrm{Re} = 1250$, where it disappears (almost certainly in a turning-point bifurcation), and one

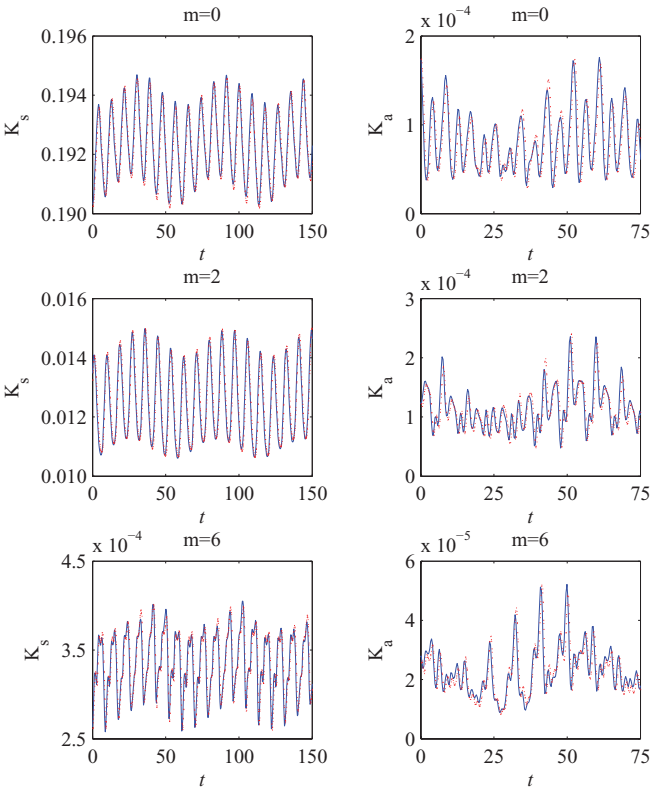

FIG. 13. (Color online) The kinetic energy in the Fourier modes $m = 0$, 2, and 6 as functions of time, for the mixed-parity $\mathrm{Re} = 1270$ quasiperiodic solution. The left column shows K_s, and the right column K_a. The solid (blue) curves are the H2000 results, and the dotted (red) curves the SFEMANS results.

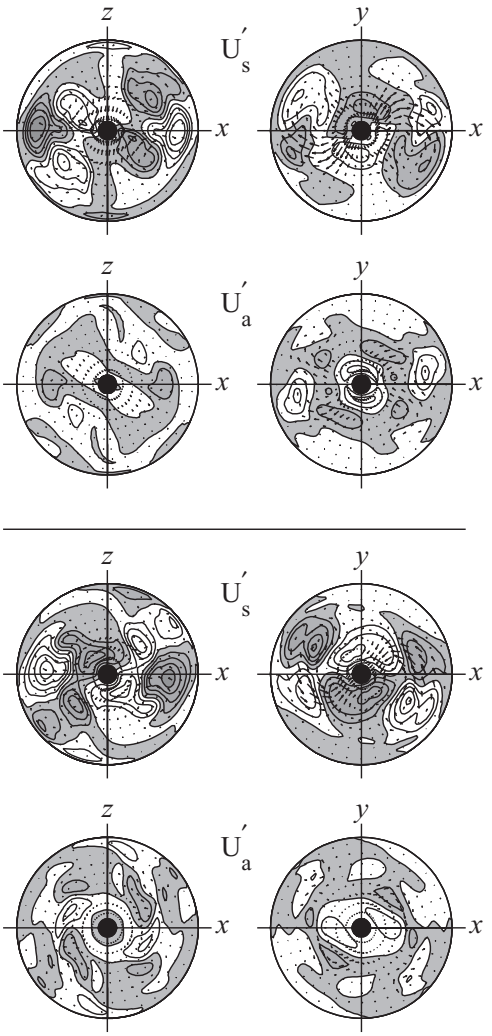

FIG. 14. Two snapshots of $\mathbf{U}'$ for the Re = 1270 mixed-parity solution, at the instants in time where K_s, $m = 0$ has its maximum and minimum values near $t = 50$ in Fig. 13. As in Figs. 7 and 10, within each snapshot the first row shows the $\mathbf{U}'_s$ part of $\mathbf{U}'$ and the second $\mathbf{U}'_a$. The contour interval is 0.02 (as in Figs. 7 and 10, but half that in Fig. 12).

switches back to the pure-parity branch. At least over the range $1250 \leqslant \mathrm{Re} \leqslant 1280$ there are thus two branches, both quasiperiodic, but one pure parity and one mixed parity.

Figure 11 presents the time series of the kinetic energy in selected Fourier modes for the pure-parity solution, at Re = 1270. The agreement between H2000 and SFEMANS is again essentially perfect, particularly considering that this is a quasiperiodic solution, and the two codes were not started off with the same initial conditions, and were therefore not synchronized with respect to the precise point in the quasiperiodic cycle. The procedure used to generate Fig. 11 was to first run both codes long enough that each one had settled in to its own quasiperiodic solution, then run a further $t \approx 700$, then shift the two series relative to each other to obtain a particularly good fit. The spatial structure of this solution is similar to previous ones. $\bar{\mathbf{U}}$ is again virtually identical to Fig. 9, and is therefore not shown. Figure 12 shows snapshots of $\mathbf{U}'$, which may be compared in particular with Fig. 4.

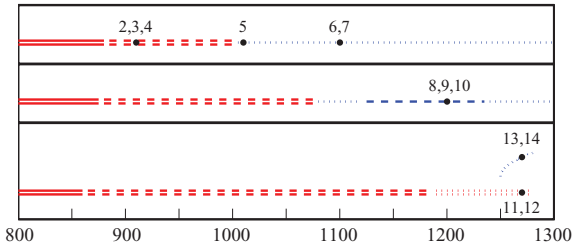

FIG. 15. (Color online) Schematic bifurcation diagrams of the solutions obtained for no inner core (top), stress-free inner core (middle), and no-slip inner core (bottom). The Reynolds number is plotted on the horizontal axis, but the vertical "axis" does not correspond to any particular quantity. Double lines (red) indicate symmetric solutions, and single lines (blue) asymmetric. Solid lines (red only) indicate steady solutions, dashed (red and blue) periodic solutions, and dotted (red and blue) quasiperiodic solutions. The black dots, and the numerals beside them, denote the corresponding figures showing aspects of these solutions.

Finally, Figs. 13 and 14 show the equivalent of Figs. 11 and 12, but for the mixed-parity solution at Re = 1270. At first sight the agreement between H2000 and SFEMANS might appear slightly less than perfect now, but we recall that these are also quasiperiodic solutions, so unless one compares sufficiently long time series to be able to match up the right points in the cycle, one should expect at least a few slight differences. Figure 14 again shows similar spatial structures to Figs. 7 and 10.

VII. CONCLUSION

In this paper we have demonstrated that even an inner sphere as small as 1/10 the radius of the outer sphere can have a surprisingly large effect on the details of the bifurcations obtained as the Reynolds number is increased. Taken together, the three cases no inner core, stress-free, and no-slip inner core exhibit a rich variety of possible solutions, including (a) periodic, pure parity (Fig. 2), (b) periodic, mixed parity (Fig. 8), (c) quasiperiodic, pure parity (Fig. 11), and (d) quasiperiodic, mixed parity (Figs. 5, 6, and 13). Figure 15 summarizes the solutions obtained in the three different cases. Because all of these solutions have been obtained with two very different and independently developed codes, they may also be useful as benchmarks for other Navier-Stokes solvers.

There is also considerable further work that could be done. First, remaining within the confines of the study presented here, it would be of interest to further increase Re, particularly in the no-slip inner core case in Sec. VI. Second, the three parameters that were fixed here, $\epsilon = 0.3$, $\alpha = 120°$, and $r_i = 0.1$, could also be varied. It is very likely that the full four-dimensional parameter space contains further interesting solutions waiting to be discovered. Finally, following Refs. [26–28], one could investigate the possible dynamo action of some of these solutions.

ACKNOWLEDGMENTS

R.H. and S.V. are supported at ETH Zürich by ERC Grant No. 247303 (MFECE); P.M. was supported by Swiss

National Science Foundation Grant No. 200021-113466. Computations were done on the ETH Brutus cluster, the Swiss National Supercomputing Centre, the IBM Power 6 cluster of Institut du Développement et des Ressources en Informatique Scientifique (IDRIS, Orsay, France) (project 0254), and on the cluster at Texas A&M University. C.N., F.L., and J.L. acknowledge helpful discussions with J.-L. Guermond.

[1] T. Sloudsky, Bull. Soc. Imp. Nat. **9**, 285 (1895).
[2] H. Poincaré, Bull. Astron. **27**, 321 (1910).
[3] K. Stewartson and P. H. Roberts, J. Fluid Mech. **17**, 1 (1963).
[4] F. H. Busse, J. Fluid Mech. **33**, 739 (1968).
[5] S. Kida, J. Fluid Mech. **680**, 150 (2011).
[6] E. C. Bullard, Proc. R. Soc. London, Ser. A **197**, 433 (1949).
[7] W. V. R. Malkus, Science **160**, 259 (1968).
[8] R. R. Kerswell, Geophys. Astrophys. Fluid Dyn. **72**, 107 (1993).
[9] C. C. Wu and P. H. Roberts, Geophys. Astrophys. Fluid Dyn. **105**, 287 (2011).
[10] J. Vanyo, P. Wilde, P. Cardin, and P. Olson, Geophys. J. Int. **121**, 136 (1995).
[11] J. P. Vanyo and J. R. Dunn, Geophys. J. Int. **142**, 409 (2000).
[12] J. Noir, D. Brito, K. Aldridge, and P. Cardin, Geophys. Res. Lett. **28**, 3785 (2001).
[13] J. Noir, P. Cardin, D. Jault, and J. P. Masson, Geophys. J. Int. **154**, 407 (2003).
[14] D. Cebron, M. Le Bars, and P. Meunier, Phys. Fluids **22**, 116601 (2010).
[15] S. Goto, N. Ishii, S. Kida, and M. Nishioka, Phys. Fluids **19**, 061705 (2007).
[16] S. Kida and N. Nakazawa, Theor. Comput. Fluid Dyn. **24**, 259 (2010).
[17] S. A. Triana, D. S. Zimmerman, and D. P. Lathrop, J. Geophys. Res. B **117**, 804103 (2012).
[18] R. R. Kerswell, J. Fluid Mech. **321**, 335 (1996).
[19] A. Tilgner, J. Fluid Mech. **379**, 303 (1999).
[20] J. Noir, D. Jault, and P. Cardin, J. Fluid Mech. **437**, 283 (2001).
[21] A. Tilgner and F. H. Busse, J. Fluid Mech. **426**, 387 (2001).
[22] S. Lorenzani and A. Tilgner, J. Fluid Mech. **447**, 111 (2001).
[23] S. Lorenzani and A. Tilgner, J. Fluid Mech. **492**, 363 (2003).
[24] S. Kida, K. Nakayama, and N. Honda, Fluid Dyn. Res. **41**, 011401 (2009).
[25] K. Zhang, K. H. Chan, and X. Liao, Phys. Fluids **22**, 116604 (2010).
[26] A. Tilgner, Phys. Fluids **17**, 034104 (2005).
[27] A. Tilgner, Geophys. Astrophys. Fluid Dyn. **101**, 1 (2007).
[28] C. C. Wu and P. H. Roberts, Geophys. Astrophys. Fluid Dyn. **103**, 467 (2009).
[29] C. A. Dwyer, D. J. Stevenson, and F. Nimmo, Nature (London) **479**, 212 (2011).
[30] K. Glampedakis, N. Andersson, and D. I. Jones, Mon. Not. R. Astron. Soc. **394**, 1908 (2009).
[31] K. Stewartson and J. R. A. Rickard, J. Fluid Mech. **35**, 759 (1970).
[32] M. Rieutord, S. A. Triana, D. S. Zimmerman, and D. P. Lathrop, Phys. Rev. E **86**, 026304 (2012).
[33] R. R. Kerswell, J. Fluid Mech. **298**, 311 (1995).
[34] R. Hollerbach and R. R. Kerswell, J. Fluid Mech. **298**, 327 (1995).
[35] C. Jones, P. Boronski, A. Brun, G. Glatzmaier, T. Gastine, M. Miesch, and J. Wicht, Icarus **216**, 120 (2011).
[36] J. L. Guermond, J. Léorat, F. Luddens, and C. Nore, Eur. J. Mech. B **39**, 1 (2013).
[37] R. Hollerbach, Inter. J. Numer. Methods Fluids **32**, 773 (2000).
[38] J. L. Guermond, R. Laguerre, J. Léorat, and C. Nore, J. Comp. Physics **228**, 2739 (2009).
[39] C. Sovinec, A. Glasser, T. Gianakon, D. Barnes, R. Nebel, S. Kruger, D. Schnack, S. Plimpton, A. Tarditi, and M. Chu, J. Comp. Physics **195**, 355 (2004).
[40] A. Fournier, H. P. Bunge, R. Hollerbach, and J. P. Vilotte, J. Comp. Physics **204**, 462 (2005).
[41] C. Nore, J. Léorat, J. L. Guermond, and F. Luddens, Phys. Rev. E **84**, 016317 (2011).
[42] P. Marti, Ph.D. thesis, ETH Zürich, 2012.
[43] S. Vantieghem, Ph.D. thesis, Université Libre de Bruxelles, 2011.
[44] P. Marti, N. Schaeffer, R. Hollerbach, D. Cebron, C. Nore, F. Luddens, J-L. Guermond, J. Aubert, Y. Sasaki, S. Takehiro, Y. Hayashi, R. Simitev, F. Busse, S. Vantieghem, and A. Jackson (unpublished).